Shock-induced incongruent melting of olivine in Kamargaon L6 chondrite

Kishan Tiwari[1, *]**, Sujoy Ghosh**[1]**, Masaaki Miyahara**[2]**, Dwijesh Ray**[3]

[1]Department of Geology and Geophysics, Indian Institute of Technology, Kharagpur - 721302, India

[2]Graduate School of Advanced Science and Engineering, Hiroshima University, Higashi-Hiroshima, Hiroshima 739-8526, Japan

[3]Planetary Sciences Division, Physical Research Laboratory, Ahmedabad – 380009, India

Corresponding author: kishantiwari@iitkgp.ac.in

Key Points:

- We report shock-induced incongruent melting of olivine in an ordinary chondrite for the first-time
- Olivine first dissociated to magnesiowüstite and liquid followed by crystallization of orthoenstatite from the residual liquid
- Olivine grains may have experienced pressure and temperature of ~25 GPa and ~2500 °C

Abstract

Here we report for the first-time shock-induced incongruent melting of olivine in an ordinary chondrite. Several olivine grains (Fo_{74}), entrained in the shock-melt vein of the Kamargaon L6 chondrite were dissociated into magnesiowüstite (X_{Fe} = 0.71) and orthoenstatite (X_{Fe} = 0.22). We propose that the breakdown of olivine took place as a result of incongruent melting to produce magnesiowüstite and Mg-rich liquid. We suggest that bridgmanite may have crystallized as the second phase from the olivine melt which back transformed to a low-pressure phase of orthoenstatite from subsequent high-temperature and low pressure events. In this case, olivine grains may have experienced pressure and temperature of ~25 GPa and ~2500 °C, respectively. Our results suggest that the incongruent melting of olivine may possibly be operated as one of the alternative mechanisms of dissociation reaction driving the phase transformation in the Earth's lower mantle.

Plain language summary

The planet Earth was formed from the similar material that constitutes present-day asteroids which is mostly made up of olivine. Therefore, it is important to study olivine at high pressure and high temperature to understand its behavior. Olivine breaks down into bridgmanite and magnesiowüstite in the Earth's mantle which is one of the most important reactions that largely controls the physical and chemical properties of the Earth's interior. This breakdown may occur where the olivine remains in the solid-state or may also form by melting of the olivine. The breakdown assemblage of bridgmanite and magnesiowüstite formed by both the mechanisms and has been reported in few Martian meteorites. Recently, this breakdown assemblage by the solid-state has been reported in the Suizhou meteorite. However, no such assemblage formed by melting has been found in meteorites originated from the asteroid belt. We, for the first time, report the possible occurrence of bridgmanite

and magnesiowüstite formed by incongruent melting of olivine in an ordinary chondrite. This assemblage may have formed at pressure and temperature of ~25 GPa and ~2500 °C. These observations suggest that the dissociation of olivine in the Earth's mantle can also take place by the melting of olivine.

1. Introduction

Olivine is volumetrically the most important phase of the Earth's upper mantle, that undergoes successive pressure-dependent solid-state transformations to wadsleyite (modified spinel structure) at 410-km and then to ringwoodite (spinel structure) at 520-km (Ringwoodite, 1991; Frost, 2008) and ultimately breaks down to form bridgmanite plus magnesiowüstite at 660-km (Ito & Takahashi, 1989). In addition, high-pressure experiments suggest that olivine melts incongruently into magnesiowüstite and liquid at above 8 GPa and 2100 ^{o}C (Presnall & Walter, 1993; Kato et al., 1998; Ohtani et al., 1998) because a compositionally equivalent mixture of magnesiowüstite and liquid has lower free energy than olivine melt at high-pressures (Matsui & Kawamura, 1980; Syono et al., 1981). Therefore, the dissociation mechanism of olivine is pivotal to understand the dynamics of the interior of the Earth and other terrestrial planets because it affects the physical and chemical properties such as densities and elastic velocities of mantle materials.

Shock-induced features including high-pressure phase transformations, dissociation reactions, and melting textures are primarily driven by high-pressure and high-temperature (HP-HT) conditions produce via high-velocity collisions among asteroid parent bodies and impact events on the Moon and Mars. Most of the high-pressure phases in shocked meteorites occur in and around shock-induced melt veins (e.g., Tomioka & Miyahara, 2017). The solid-state polymorphic transformation of olivine to wadsleyite and ringwoodite have been reported in chondrites (Binns et al., 1979; Ohtani et al., 2004; Xie & Sharp, 2007; Weisberg & Kimura, 2010; Miyahara et al., 2010), Martian meteorites (Greshake et al., 2013; Walton et al., 2014; Miyahara et al., 2016) and lunar meteorites (Barrat et al., 2005; Zhang et al., 2010). Whereas, olivine grains in contact with the matrix of melt veins and melt pockets of shocked shergottites (DaG 735 and Tissint) have been dissociated to vitrified bridgmanite + ferropericlase (Miyahara et al., 2011, 2016; Walton et al., 2014). Recently, Bindi et al.,

81 (2020) reported dissociation of Fe-rich olivine (X_{Fe} = 0.52) to hiroseite (Fe-rich bridgmanite,
82 X_{Fe} = 0.59) and ferropericlase (X_{Fe} = 0.44) by the solid-state transformation in the Suizhou
83 L6 chondrite. However, natural dissociation of olivine by incongruent melting has, to date,
84 not been observed in shocked ordinary chondrites.

85 The Kamargaon meteorite fell on 13th November, 2015 near the town of Kamargaon,
86 which is located 27 km away from the Golaghat district of Assam, India (Goswami et al.,
87 2016) and was classified as an L6 chondrite (Ray et al., 2017). Previous studies on
88 Kamargaon L6 chondrite described olivine, pyroxene, plagioclase, and metal-sulfide
89 (kamacite, taenite, and troilite) as major rock-forming minerals, whereas chromite as an
90 accessory phase in the chondritic portion (Goswami et al., 2016; Ray et al., 2017). Ray et al.
91 (2017) calculated U-Th-^{4}He, and K-Ar radiometric ages and cosmic ray exposure age of
92 Kamargaon L6 chondrite. The bulk trace element analyses of Kamargaon L6 chondrite
93 suggest LREE enrichment as compared to other L chondrites (Saikia et al., 2017). The
94 mineralogical and textural analysis of shock-melt veins (SMVs) of Kamargaon L6 chondrite
95 has not been studied yet. In the present study, we carefully examined SMV present in the
96 Kamargaon L6 chondrite to understand dissociation and melting textures displayed by olivine
97 grains and their formation mechanisms which further provide clues to estimate the shock
98 conditions in the chondrite parent body.
99

100 **2. Materials and methods**

101 A small piece (~2g) of Kamargaon chondrite was embedded in a low-viscosity epoxy
102 resin and its surface was polished using diamond paste. Preliminary textural observation and
103 phase identification was done using a scanning electron microscope (SEM) JEOL JSM-6490
104 installed at Indian Institute of Technology (IIT) Kharagpur, equipped with energy-dispersive
105 spectrometer (EDS) operating at an acceleration voltage of 15 kV. The fine textural variations

and associations of different phases were investigated using a field emission gun scanning electron microscope (FEG-SEM) using a JEOL JSM-7000F at Tohoku University, with an acceleration voltage of 15 kV.

The chemical compositions of the various phases observed in Kamargaon L6 chondrite were obtained by electron probe microanalyser (EPMA) using a Cameca-SX 100 with three wavelength dispersive spectrometers (WDS) operating at an accelerating potential of 15kV at Physical Research Laboratory (PRL), Ahmedabad. To minimize the beam damage and loss of alkali elements, we analysed feldspar grains with the beam current and probe diameter of 10 nA and 5 µm, respectively, whereas all the other phases were analysed with a beam current of 15 nA and minimum beam diameter (~1 µm). Minimum counting times were 20s on the peak and 10s on each side of the background. The following natural silicates, sulfides and metal standards were used for calibration: diopside and plagioclase (Si), rutile (Ti), kyanite (Al), wollastonite (Ca), almandine (Fe in silicates), iron metal (Fe in metal and sulfide phase), olivine (Mg), rhodonite (Mn), jadeite (Na), orthoclase (K), apatite (P), pyrite (S), chromite (Cr), nickel metal (Ni), cobalt metal (Co), vanadium metal (V). The data were corrected for absorption, fluorescence, and atomic number effects using routine PAP (a Phi-Rho-Z correction technique) procedure.

Different mineral phases and their polymorphs were identified using a laser micro-Raman spectrometer, Horiba Jobin-Yvon LabRam HR800 at Indian Institute of Science Education and Research (IISER) Kolkata, India. A microscope was used to focus the excitation laser beam (a He-Ne laser, 633 nm line with 1800 L /mm grating). Laser power on a sample was kept at 7.5 mW and the acquisition times were 10–30 s. For each phase, a Raman shift was acquired in the spectral region of 200–1200 cm^{-1}.

129 Slice for TEM observations were prepared by a Focused Ion Beam (FIB) system
130 using a JEOL 9320-FIB at Tohoku University. A gallium ion beam was accelerated to 30 kV
131 during the sputtering of the slice, and the slice was approximately 100 nm in thickness. A
132 JEOL JEM-2100F filed-emission (FE)-TEM operating at 200 kV with a JEOL energy-
133 dispersive X-ray spectroscopy (EDS) detector system was used for conventional TEM
134 observation and selected area electron diffraction (SAED) analyses at Tohoku University. We
135 determined the chemical composition of each mineral under the scanning TEM (STEM)
136 mode with the EDS detector. The chemical compositions were corrected using
137 experimentally determined k-factors [albite, pyrope, almandine, San Carlos olivine, and
138 synthetic (Mg,Fe)O].

139 **3. Results**

140 The host rock of the Kamargaon L6 chondrite mainly consists of olivine (Fo_{73-74}),
141 low-calcium pyroxene ($En_{77-80}Fs_{19-22}Wo_{1-2}$), high-calcium pyroxene ($En_{45-46}Fs_{9-10}Wo_{44-46}$),
142 plagioclase ($Ab_{62-70}An_{18-23}Or_{12-15}$), Fe-Ni metal alloy (kamacite and taenite), troilite and a
143 minor amount of phosphate and chromite. The mid-portion of the sample consists of a major
144 thick SMV ranging in width from ~700 to 1600 μm. We observed that numerous olivine
145 grains entrained in the SMV have been dissociated into fine-grained granular assemblage.
146 The extent of dissociation of olivine grains seems to be dependent on the grain size and
147 location of grains in the SMV. The grains which are relatively coarser (>100 μm across)
148 and/or occur near the SMV-host rock boundary (vein edge) are partially dissociated and
149 exhibit heterogeneous texture and composition (Figs. 1a-b). Whereas the grains which are
150 finer (<100 μm across) and/or in the mid-portion of the SMV have been completely
151 dissociated (Fig. 1c). Partially dissociated olivine grains show dissociation texture as well as
152 vesicular texture and the core part of such grains displays vesicular texture. Whereas the
153 outer rim part of the grain exhibits dissociation texture. Spherulitic texture is common in

between them (Fig. 1b). The Raman spectra of these dissociated olivine grains exhibit two strong peaks at ~821 (DB1) and ~853 (DB2) cm^{-1} corresponding to characteristic doublet attributed to symmetric and asymmetric stretching vibrations of Si-O bond in SiO_4 tetrahedra in olivine structure (McMillan & Akaogi., 1987) and apparently relatively a weak, less sharp peak at ~664 cm^{-1} indicates the presence of pyroxene glass (Fig. 2) (Kubicki et al., 1992). These measured Raman spectra were used to measure the composition of the residual olivine that escaped the dissociation. The forsterite content of the residual olivine was established using olivine of terrestrial, meteoritic and synthetic origin by combining the doublet (DB1 and DB2) peak positions (Kuebler et al., 2006):

$$Fo = (80.19x_1 + 399.35x_2 - 0.04x_1^2 - 0.24x_2^2 - 206232.99) \times 100 \quad (1)$$

where Fo is forsterite content, x_1 and x_2 are peak positions of DB1 and DB2, respectively. Using this relationship, calculated Fo content of the residual olivine in Kamargaon L6 chondrite is ~75 ±10. The Raman spectra of the olivine grains present in the host rock show a strong doublet at peak positions of ~820.4 and ~851.4 cm^{-1} (Fig. 2). Their Fo contents calculated from Eq. (1) of ~75 ±10 and match well with measured Fo content of the host olivine grains of ~74 using electron probe micro analyzer (Table 1). This suggests that the calculated Fo contents of dissociated olivine using Raman data holds good for our sample.

A thin slice (~20 × 7 × 10 μm) of a bean shaped (~92 × 40 μm) completely dissociated olivine grain in the SMV, adjacent to the vein edge (Fig. 1c) was excavated by a FIB system and analyzed using a TEM to further investigate the assemblage and microtextures of dissociated olivine. A high angle annular dark field (HAADF) image of the TEM slice and STEM EDS analysis exhibit micro porphyritic texture where bright euhedral grains with (Mg,Fe)O composition are embedded in grey matrix consisting of $(Mg,Fe)SiO_3$ (Fig. 3a-b, Table 1). The selected area electron diffraction (SAED) patterns confirm that the

bright grains are magnesiowüstite indexed to cubic structure with a = 4.376 Å (Fig. 3c) and the grey matrix is orthorhombic enstatite (hereafter orthoenstatite) with b = 10.27 Å (Fig. 3d). The magnesiowüstites are dimensionally much larger (up to ~500 nm across) than the elongated orthoenstatites (~50 nm × ~200 nm). The elongated microlites of orthoenstatite grains display dendritic texture (Fig. 3b) which radiates perpendicularly outwards from individual magnesiowüstites. TEM-EDS analyses shows that magnesiowüstite ($Mg_{0.3}Fe_{0.7}O$) have X_{Fe} [molar Fe/(Fe+Mg)] of 0.71 whereas orthoenstatite ($Mg_{1.85}Fe_{0.25}Si_{1.9}O_6$) have X_{Fe} of 0.12 (Table 1).

4. Discussion

Dissociated assemblage of bridgmanite and magnesiowüstite in high-pressure experiments (Frost and Langenhorst, 2002; Sinmyo et al., 2008) and Martian meteorites (DaG 735 and Tissint, Miyahara et al., 2011, 2016) shows equigranular texture with ~120° triple junctions between coexisting bridgmanite and magnesiowüstite grain. These textures have been interpreted to be the evidence of the solid-state transformation due to the simultaneous and random nucleation as well as crystal growth of the coexisting phases. Whereas, a dissociated assemblage of bridgmanite and magnesiowüstite resulting from incongruent melting in high-pressure experiments (Kato et al., 1998; Ohtani et al., 1998) and Martian meteorite (NWA 2737, Miyahara et al., 2019) displays normally euhedral to subhedral grains of the first liquidus phase. While the subsequent second liquidus phase is relatively fine grained compared to early formed phase and occupy the interstitial space. Thus, incongruent melting of olivine results in porphyritic texture where the dimensionally larger grains of phenocrysts are generally the first liquidus phase. Dissociated olivines in the Kamargaon L6 chondrite show micro-porphyritic texture with no triple junctions along the grain boundaries. Therefore, we propose that the dissociation assemblage is as a result of the

melting of olivine. We carefully examine the texture and Raman spectra of the dissociated part of olivine to test two possibilities for the formation of orthoenstatite: (1) crystallization of orthoenstatite directly from the melt, and (2) crystallization of bridgmanite from the residual melt which was back-transformed to a low-pressure phase of orthoenstatite as a result of subsequent high-temperature event.

Melting experiments in the Mg_2SiO_4-Fe_2SiO_4 system have shown that the olivine (Fa_{10}) begins to melt incongruently above 8.5 GPa and 2050 °C to magnesiowüstite and Mg-rich silicate liquid (Ohtani et al., 1998). It is likely that with increasing pressure, the incongruent melting temperature of olivine increases but decreases by the addition of fayalite component. We observed that the fayalite content of olivine present in the host rock of Kamargaon is higher (Fa_{26}) than that of the synthetic olivine used by Ohtani et al. (1998). Therefore, we infer that the olivine grains were partially or completely melted incongruently to produce magnesiowüstite and melt, followed by crystallization of orthoenstatite from the residual melt. These orthoenstatites may have crystallized directly from the residual liquid during rapid cooling as indicated by dendritic texture. The heterogeneity in degree of incongruent melting may possibly be because of the development of temperature gradient in the olivine grains entrained in SMVs as their outer surface is in direct contact with shock melt which makes their inner core portion relatively cooler.

Crystalline structure of natural bridgmanite (X_{Mg} = 0.78) reported in shocked Tenham L6 chondrite that are coexisting with akimotoite (Tschauner et al., 2013). These fine-grained polycrystalline bridgmanite are formed by the solid-state phase transformation from orthoenstatite. Most of the bridgmanite reported in shocked meteorites are found in vitrified state (Sharp et al. 1997; Tomioka and Fujino 1997; Tomioka and Kimura, 2003; Chen et al. 2004a; Xie et al. 2006) due to the following reasons: (1) bridgmanite becomes unstable at high post-shock temperature after decompression (Durben and Wolf, 1992; Kubicki et al.,

1992), (2) it may also get easily damaged by ion sputtering during FIB sample preparation, and (3) under electron beam bombardment in TEM analysis (Sharp et al. 1997; Tomioka and Fujino 1997). In the present study, no such vitrified phase is observed in the dissociated grains of olivine in Kamargaon. However, orthoenstatite coexisting with magnesiowüstite is identified as a dissociation product of olivine. The Raman spectra from the dissociated portion indicate the presence of pyroxene glass (Fig. 2) although we did not find any vitrified phase with $(Mg,Fe)SiO_3$ composition in the part excavated for TEM observation. Miyahara et al. (2011) observed a similar Raman peak at 665 cm^{-1} from the dissociated olivine in Martian meteorite (DaG 735) and interpreted that it corresponds to vitrified bridgmanite. Thus, the Raman peak at 664 cm^{-1} we observed from the dissociated portion of shocked Kamargaon L6 chondrite might correspond to the remnant of vitrified bridgmanite that was absent in the portion analyzed by TEM. Forsteritic olivine (Fa_{10}) melts incongruently to magnesiowüstite and liquid at 23 GPa but the assemblage changes to magnesiowüstite and bridgmanite at ~25 GPa and ~2500 °C (Ohtani et al., 1998). It is likely that the incongruent melting of olivine took place at or above the pressure of 25 GPa and magnesiowüstite and bridgmanite were crystallized as the dissociation product. The bridgmanite may have later back-transformed to a low-pressure phase of orthoenstatite as a result of subsequent high temperature event. In this case, olivine grains may have experienced similar pressure and temperature of ~25 GPa and ~2500 °C, respectively. Such occurrence of back transformed pyroxene and magnesiowüstite assemblage has been reported as inclusions in sublithospheric diamonds (Hutchison et al., 2001; Zedgenizov et al., 2020). We also calculated the modal proportion of orthoenstatite and magnesiowüstite in the Kamargaon L6 chondrite using the image analysis software (ImageJ) and estimated that the ratio is 69:31 for orthoenstatite and magnesiowüstite which is very similar to the modal proportion of bridgmanite and magnesiowüstite formed by the solid-state transformation in high-pressure experiments and the Martian meteorite of DaG

735 (Ito & Takahashi 1989; Miyahara et al., 2011). Further, extra-terrestrial olivine studied here is slightly Fe-rich (Fa_{26}) compared to olivine (Fa_{8-12}) from the upper mantle. In addition, dissociation mechanism of Kamargaon olivine, i.e., incongruent melting, is different from the solid-state dissociation mechanism of olivine expected in the Earth's mantle. However, natural evidence of dissociation of olivine by incongruent melting to lower mantle assemblage and the resulting similar modal ratio of coexisting phases to that of the solid-state dissociation compels us to consider incongruent melting of olivine as possibly one of the alternative mechanisms driving the phase transformation in the transition zone and lower mantle.

5. Conclusions

Here we report the first occurrence of olivine dissociated into magnesiowüstite and orthoenstatite in the shocked Kamargaon L6 chondrite, a meteorite that originated from the asteroids. Based on the textural observations, we suggest that this dissociated assemblage formed by incongruent melting of olivine into magnesiowüstite and Mg-rich melt. The orthoenstatite was the second phase to crystallize from the residual melt. We propose two possible scenarios for the origin of this assemblage on the basis of textural evidence and Raman spectra: **(1)** the incongruent melting took place at or above the pressure and temperature of ~8.5 GPa and ~2050 °C to produce magnesiowüstite and Mg-rich melt and orthoenstatite subsequently crystallized from the melt under rapid cooling and low pressure, and **(2)** the incongruent melting took place at or above the pressure and temperature of ~25 GPa and ~2500 °C to produce magnesiowüstite and Mg-rich melt and subsequently bridgmanite crystallized from the melt. In the latter case, we suggest that bridgmanite was heated and back transformed to low pressure phase of orthoenstatite as a result of subsequent high-temperature and low-pressure event. These observations point towards the possibility of

277 incongruent melting operating as an alternate mechanism for phase transformation in the
278 Earth's lower mantle.
279
280 **Acknowledgments**
281 S.G. acknowledges the financial support by Council of Scientific and Industrial Research
282 (CSIR) grant 24(0362)/20/EMR-II. K.T. acknowledges the support for his Ph.D. fellowship
283 from University Grants Commission, Govt. of India. All the data used in this study, including
284 all the figures (Fig. 1 to 3) and table (Table 1) in this manuscript, can be accessed through the
285 following DOI: https://doi.org/10.6084/m9.figshare.14341772.v1
286
287 **References**
288 Barrat, J. A., Chaussidon, M., Bohn, M., Gillet, P., Göpel, C., & Lesourd, M. (2005). Lithium
289 behavior during cooling of a dry basalt: An ion-microprobe study of the lunar meteorite
290 Northwest Africa 479 (NWA 479). *Geochimica et Cosmochimica Acta*, 69(23), 5597-
291 5609. DOI: 10.1016/j.gca.2005.06.032

292 Binns R. A., Davis R. J., & Reed S. J. B. (1969). Ringwoodite, natural $(Mg,Fe)_2SiO_4$ spinel
293 in the Tenham meteorite. *Nature*, 221, 943–944. DOI:10.1038/221943a0

294 Bindi, L., Shim, S. H., Sharp, T. G., & Xie, X. (2020). Evidence for the charge
295 disproportionation of iron in extraterrestrial bridgmanite. *Science advances*, 6(2),
296 eaay7893. DOI: 10.1126/sciadv.aay7893

297 Chen M., Xie, X. & Goresy, A. E. (2004). A shock-produced $(Mg,Fe)SiO_3$ glass in the
298 Suizhou meteorite. *Meteoritics and Planetary Science*, 39: 1797-1808.
299 DOI:10.1111/j.1945-5100.2004.tb00076.x

300 Durben, D. J., & Wolf, G. H. (1992). High-temperature behavior of metastable $MgSiO_3$
301 perovskite: a Raman spectroscopic study. *American Mineralogist*, 77(7-8), 890-893.

302 Fritz, J., & Greshake, A. (2009). High-pressure phases in an ultramafic rock from Mars.
303 *Earth and Planetary Science Letters*, 288(3-4), 619-623. DOI:10.1016/j.epsl.2009.10.030

304 Frost, D.J. (2008) The upper mantle and transition zone. *Elements*, *4*(3), pp.171-176.DOI:
305 10.2113/GSELEMENTS.4.3.171

306 Frost, D. J., & Langenhorst, F. (2002). The effect of Al_2O_3 on Fe–Mg partitioning between
307 magnesiowüstite and magnesium silicate perovskite. *Earth and Planetary Science*
308 *Letters*, 199(1-2), 227-241. DOI:10.1016/S0012-821X(02)00558-7

Goswami T.K., Ray D., Sarmah R.K., Goswami U., Bhattacharyya P., Majumdar D., Bezbaruah D., & Borgohain P. (2016). Meteorite fall at Komargaon, Assam, India. *Current Science,* 110(10), 1894-1895.

Greshake A., Fritz J., BÖttger U., & Goran D. (2013). Shear induced ringwoodite formation in the Martian shergottite Dar al Gani 670. *Earth and Planetary Science Letters,* 375:383–394. DOI:10.1016/j.epsl.2013.06.002.

Hutchison, M. T., Hursthouse, M. B., & Light, M. E. (2001). Mineral inclusions in diamonds: associations and chemical distinctions around the 670-km discontinuity. *Contributions to Mineralogy and Petrology*, 142(1), 119-126. DOI:10.1007/s004100100279

Ito E. & Takahashi E. (1989). Post-spinel transformations in the system Mg_2SiO_4-Fe_2SiO_4 and some geophysical implications. *Journal of Geophysical Research: Solid Earth*, 94:10637–10646. DOI:10.1029/JB094iB08p10637

Kato, T., Nakata, N., Ohtani, E., & Onuma, K. (1998). Melting experiments on the forsterite–pyrope system at 8 and 13.5 GPa. *Physics of the earth and planetary interiors*, 107(1-3), 97-102. DOI:10.1016/S0031-9201(97)00127-1

Kubicki J. D., Hemley R. J., & Hofmeister, A. M. (1992). Raman and infrared study of pressure-induced structural changes in $MgSiO_3$, $CaMgSi_2O_6$, and $CaSiO_3$ glasses. *American Mineralogist*, 77(3-4), 258-269.

Kuebler K. E., Jolliff B. L., Wang A., & Haskin L. A. (2006). Extracting olivine (Fo-Fa) compositions from Raman spectral peak positions. *Geochimica et Cosmochimica Acta,* 70:6201–6222. DOI:10.1016/j.gca.2006.07.035

Matsui, Y., & Kawamura, K. (1980). Instantaneous structure of an $MgSiO_3$ melt simulated by molecular dynamics. *Nature*, 285, 648-649. DOI:10.1038/285648a0

McMillan, P. F., & Akaogi, M. (1987). Raman spectra of beta-Mg_2SiO_4 (modified spinel) and gamma-Mg_2SiO_4 (spinel). *American Mineralogist*, 72(3-4), 361-364.

Miyahara M., Ohtani E., El Goresy A., Ozawa S., & Gillet P. (2016). Phase transition processes of olivine in the shocked Martian meteorite Tissint: Clues to origin of ringwoodite-, bridgmanite- and magnesiowüstite-bearing assemblages. *Physics of the earth and planetary interiors,* 259:18–28. DOI:10.1016/j.pepi.2016.08.006

Miyahara M., Ohtani E., Kimura M., El Goresy A., Ozawa S., Nagase T., Nishijima M., & Hiraga K. (2010). Coherent and subsequent incoherent ringwoodite growth in olivine of shocked L6 chondrites. *Earth and Planetary Science Letters,* 295:321–327. DOI:10.1016/j.epsl.2010.04.023

Miyahara, M., Ohtani, E., Nishijima, M., & El Goresy, A. (2019). Olivine melting at high pressure condition in the chassignite Northwest Africa 2737. *Physics of the earth and planetary interiors,* 291, 1-11. DOI:10.1016/j.pepi.2019.04.001

Miyahara, M., Ohtani, E., Ozawa, S., Kimura, M., El Goresy, A., Sakai, T., Nagase, T., Hiraga, K., Hirao, N. & Ohishi, Y. (2011). Natural dissociation of olivine to (Mg,Fe)SiO_3 perovskite and magnesiowüstite in a shocked Martian meteorite. *Proceedings of the National Academy of Sciences,* 108(15), pp.5999-6003. DOI:10.1073/pnas.1016921108

Ohtani, E., Moriwaki, K., Kato, T., & Onuma, K. (1998). Melting and crystal–liquid partitioning in the system Mg_2SiO_4–Fe_2SiO_4 to 25 GPa. *Physics of the earth and planetary interiors*, 107(1-3), 75-82. DOI:10.1016/S0031-9201(97)00125-8

Ohtani, E., Kimura, Y., Kimura, M., Takata, T., Kondo, T., & Kubo, T. (2004). Formation of high-pressure minerals in shocked L6 chondrite Yamato 791384: constraints on shock conditions and parent body size. *Earth and Planetary Science Letters*, 227(3-4), 505-515. DOI:10.1016/j.epsl.2004.08.018

Presnall, D. C., & Gasparik, T. (1990). Melting of enstatite ($MgSiO_3$) from 10 to 16.5 GPa and the forsterite (Mg_2SiO_4)-majorite ($MgSiO_3$) eutectic at 16.5 GPa: Implications for the origin of the mantle. *Journal of Geophysical Research: Solid Earth*, 95(B10), 15771-15777. DOI:10.1029/JB095iB10p15771

Ray D., Mahajan, R. R., Shukla, A. D., Goswami, T. K., & Chakraborty, S. (2017). Petrography, classification, oxygen isotopes, noble gases, and cosmogenic records of Kamargaon (L6) meteorite: The latest fall in India. *Meteoritics and Planetary Science*, 52(8), 1744-1753. DOI:10.1111/maps.12875

Ringwood, A. E. (1991). Phase transformations and their bearing on the constitution and dynamics of the mantle. *Geochimica et Cosmochimica Acta*, 55(8), 2083-2110. DOI:10.1016/0016-7037(91)90090-R

Saikia, B. J., Parthasarathy, G., Borah, R. R., Satyanarayanan, M., Borthakur, R., & Chetia, P. (2017). Spectroscopy and mineralogy of a fresh meteorite fall Kamargaon (L6) chondrite. *Proceedings of the Indian National Science Academy*, 83(4), 941-948.

Sharp T.G., Lingemann C.M., Dupas C. & Stöffler D. (1997), Natural occurrence of $MgSiO_3$-ilmenite and evidence for $MgSiO_3$-perovskite in a shocked L chondrite. *Science*, 277, 352–355. DOI: 10.1126/science.277.5324.352

Sinmyo, R., Hirose, K., Nishio-Hamane, D., Seto, Y., Fujino, K., Sata, N., & Ohishi, Y. (2008). Partitioning of iron between perovskite/postperovskite and ferropericlase in the lower mantle. *Journal of Geophysical Research: Solid Earth*, 113(B11). DOI:10.1029/2008JB005730

Syono, Y., Goto, T., Takei, H., Tokonami, M., & Nobugai, K. (1981). Dissociation reaction in forsterite under shock compression. *Science*, 214(4517), 177-179. DOI:10.1126/science.214.4517.177

Tomioka N. and Miyahara, M. (2017). High-pressure minerals in shocked meteorites. *Meteoritics and Planetary Science*, 52, 2017-2039. DOI:10.1111/maps.12902

Tomioka N. and Kimura, M. (2003). The breakdown of diopside to Ca-rich majorite and glass in a shocked H chondrite. *Earth and Planetary Science Letters*, 208(3-4), pp.271-278. DOI:10.1016/S0012-821X(03)00049-9

Tomioka, N. & Fujino, K. (1997). Natural $(Mg,Fe)SiO_3$-ilmenite and-perovskite in the Tenham meteorite. *Science*, 277, 1084-1086. DOI: 10.1126/science.277.5329.1084

Tschauner, O., Ma, C., Beckett, J. R., Prescher, C., Prakapenka, V. B., & Rossman, G. R. (2014). Discovery of bridgmanite, the most abundant mineral in Earth, in a shocked meteorite. *Science*, 346(6213), 1100-1102. DOI: 10.1126/science.1259369

Walton E. L., Sharp T. G., & Hu J. (2014). Heterogeneous mineral assemblages in Martian meteorite Tissint as a result of a recent small impact event on Mars. *Geochimica et Cosmochimica Acta*, 140:334–348. DOI:10.1016/j.gca.2014.05.023

Weisberg M. K. & Kimura M. (2010). Petrology and Raman spectroscopy of high pressure phases in the Gujba CB chondrite and the shock history of the CB parent body. *Meteoritics and Planetary Science*, 45:873–884. DOI:10.1111/j.1945-5100.2010.01058.x

Xie Z. & Sharp T. G. (2007). Host rock solid-state transformation in a shock-induced melt vein of Tenham L6 chondrite. *Earth and Planetary Science Letters*, 254:433–445. DOI:10.1016/j.epsl.2006.12.001

Xie Z., Sharp T. G., and DeCarli P. S. (2006). High-pressure phases in a shock-induced melt vein of the Tenham L6 chondrite: Constraints on shock pressure and duration. *Geochimica et Cosmochimica Acta*, 70:504–515. DOI:10.1016/j.gca.2005.09.003

Zedgenizov, D., Kagi, H., Ohtani, E., Tsujimori, T., & Komatsu, K. (2020). Retrograde phases of former bridgmanite inclusions in superdeep diamonds. *Lithos*, 370, 105659. DOI:10.1016/j.lithos.2020.105659

Zhang A., Hsu W., Floss C., Li X., Li Q., Liu Y., & Taylor L. A. (2010). Petrogenesis of lunar meteorite Northwest Africa 2977: Constraints from in situ microprobe results. *Meteoritics and Planetary Science*, 45:1929–1947. DOI:10.1111/j.1945-5100.2010.01131.x

Figure descriptions

Figure 1 (a) Low magnification back-scattered electron image of the portion of SMV of Kamargaon L6 chondrite shows various completely and partially dissociated olivine grains and metal-sulfide spherules. **(b)** High magnification image of the boxed area in Fig. 1a labelled as b, shows part of the partially dissociated olivine grain. The rim portion of the grains have been dissociated whereas the core portion is vesicular and spherulitic texture. Such heterogeneous texture mainly depicts the formation of temperature gradient in olivine grains entrained in the hot melt vein. **(c)** High magnification image of the boxed area in Fig. 1a labelled as c, shows relatively finer grains which have been completely dissociated. The portions marked as TEM_1 was excavated by using FIB for the TEM analysis. Ve-Ol = vesicular olivine; Di-Ol = dissociated olivine; Sph-Ol = spherulitic olivine; SMV = shock-melt vein; HR = host rock.

Figure 2 Representative Raman spectra of dissociated (Di-Ol) and host rock olivine (HR-Ol). Raman analysis of the HR-Ol produces intense doublets at ~820 and ~851 cm^{-1} whereas the Raman spectra of Di-Ol grains display two strong peaks at ~821 (DB1) and ~853 (DB2) cm^{-1} apparently relatively a weak. Less sharp peak at ~664 cm^{-1} indicates the presence of pyroxene glass.

Figure 3 (a) High-angle annular dark field (HAADF) image of the slice cut from the portion marked in Fig. 1c shows micro-porphyritic texture where bright relatively coarser grained magnesiowüstite is set in a grey matrix of finer grained orthoenstatite. **(b)** Bright-field TEM image shows the fine textures of dissociated olivine. Fine elongated microlites of orthoenstatite consist the grey matrix in which the course magnesiowüstite grains are set. **(c)** and **(d)** are electron diffraction patterns of magnesiowüstite and orthoenstatite respectively. Mw = magnesiowüstite; En = orthoenstatite.

Table 1 Chemical composition (in wt. %) of olivine present in the host rock analyzed by EPMA and orthoenstatite and magnesiowüstite formed from dissociated olivine in shock melt vien of the Kamargaon L6 chondrite analyzed by STEM-EDS.

	EPMA		STEM-EDS[#]			
Location	HR-Ol		Di-Ol			
Phases	Ol	1σ	Oen	1σ	Mw	1σ
n	21		12		7	
SiO_2	37.48	0.47	55.40	1.77	1.55	0.35
FeO*	24.44	0.24	8.51	0.81	80.44	1.09
MnO	0.45	0.04	n.d.	n.d.	n.d.	n.d.
MgO	38.01	0.16	36.09	1.64	18.01	1.19
CaO	0.04	0.03	n.d.	n.d.	n.d.	n.d.
Total	100.42		100		100	
Cation						
Si	0.978	0.009	1.906	0.072	0.016	0.004
Fe^{2+}	0.533	0.006	0.245	0.024	0.280	0.016
Mn	0.010	0.001	-	-	-	-
Mg	1.478	0.007	1.849	0.071	0.703	0.015
Ca	0.001	0.001	-	-	-	-
Oxygen	4		6		1	
Fa	26					
$X_{Fe} \times 100$			12		71	

X_{Fe} = Fe/(Mg+Fe); Oen = orthoenstatite, Mw = magnesiowüstite; Di-Ol = dissociated olivine; HR-Ol = host rock olivine; # = Total is normalized to 100 %; * = All iron is assumed to be ferrous, n = number of analyses; 1σ = standard deviation, n.d. = not determined.

Figure 1.

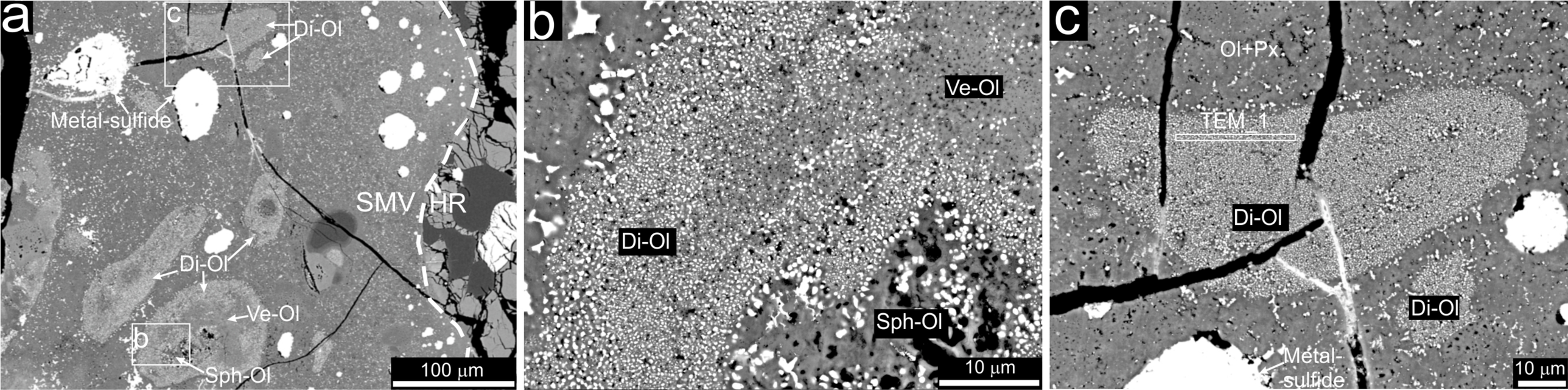
a
c
Di-Ol
Metal-sulfide
SMV
HR
Di-Ol
Ve-Ol
b
Sph-Ol
100 μm
b
Ve-Ol
Di-Ol
Sph-Ol
10 μm
c
Ol+Px
TEM_1
Di-Ol
Di-Ol
Metal-
sulfide
10 μm

Figure 2.

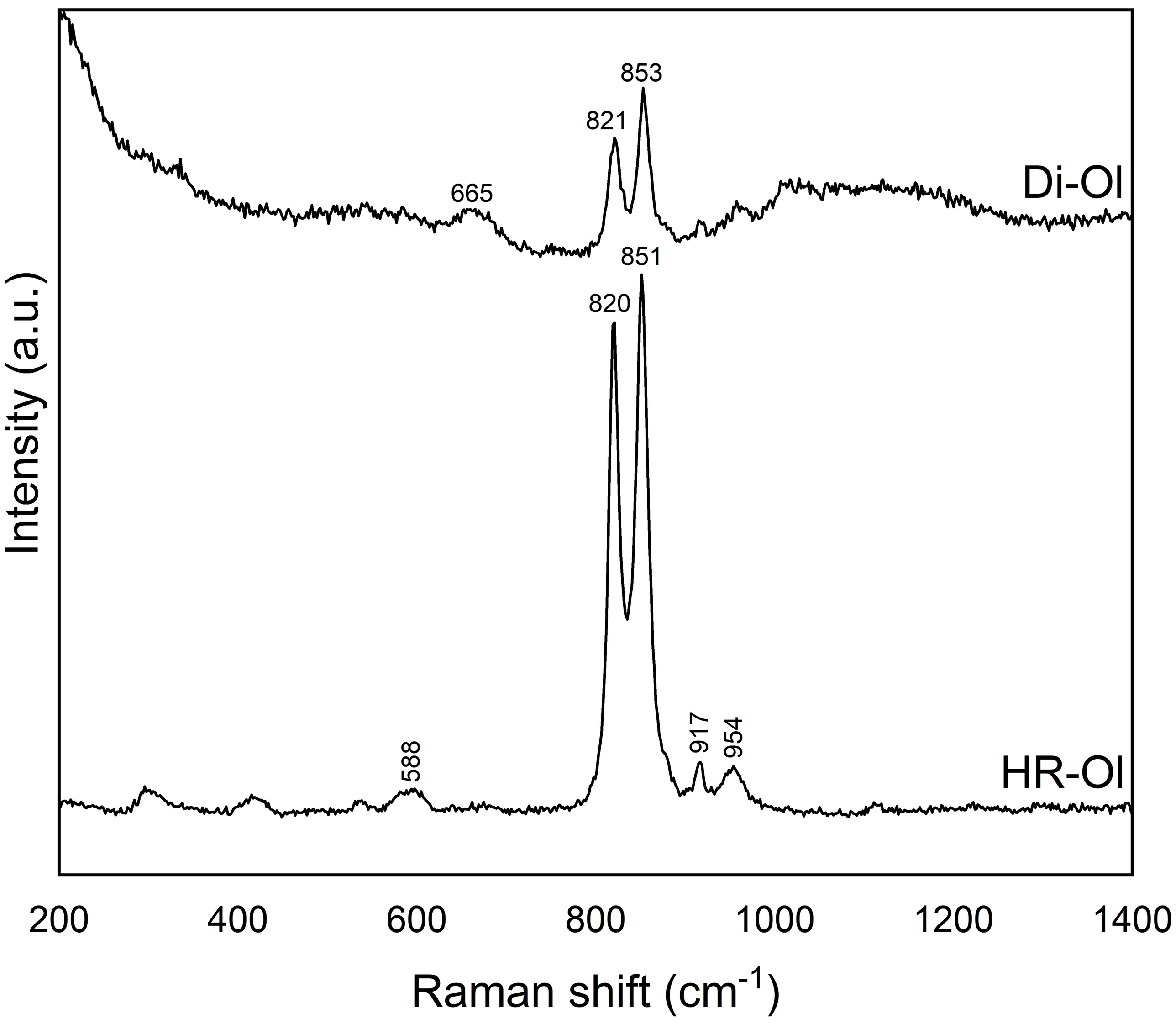
Intensity (a.u.)
853
821
665
Di-Ol
851
820
588
917
954
HR-Ol
200
400
600
800
1000
1200
1400
Raman shift (cm-1)

Figure 3.

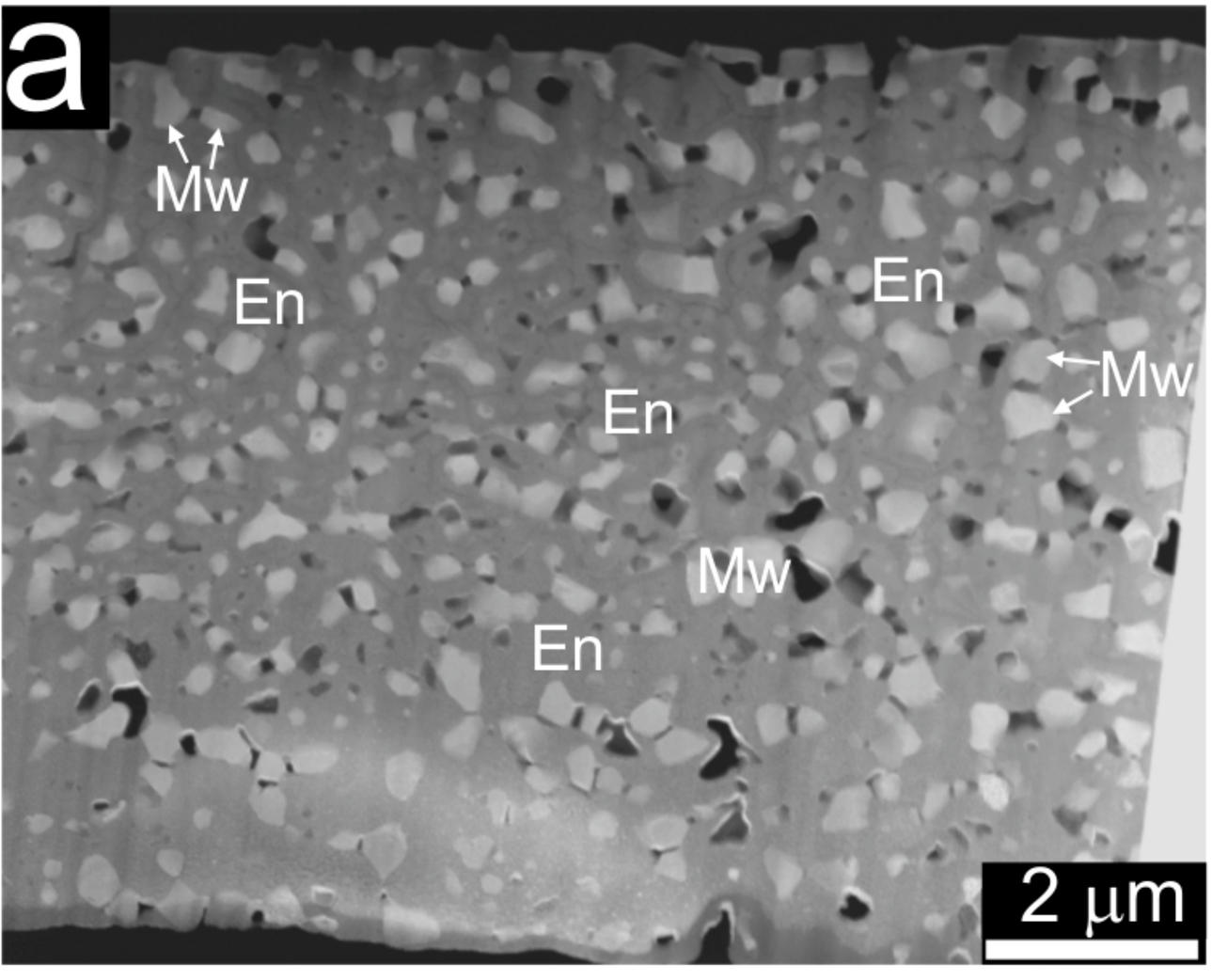
a
Mw
En
En
Mw
En
Mw
En
2 μm

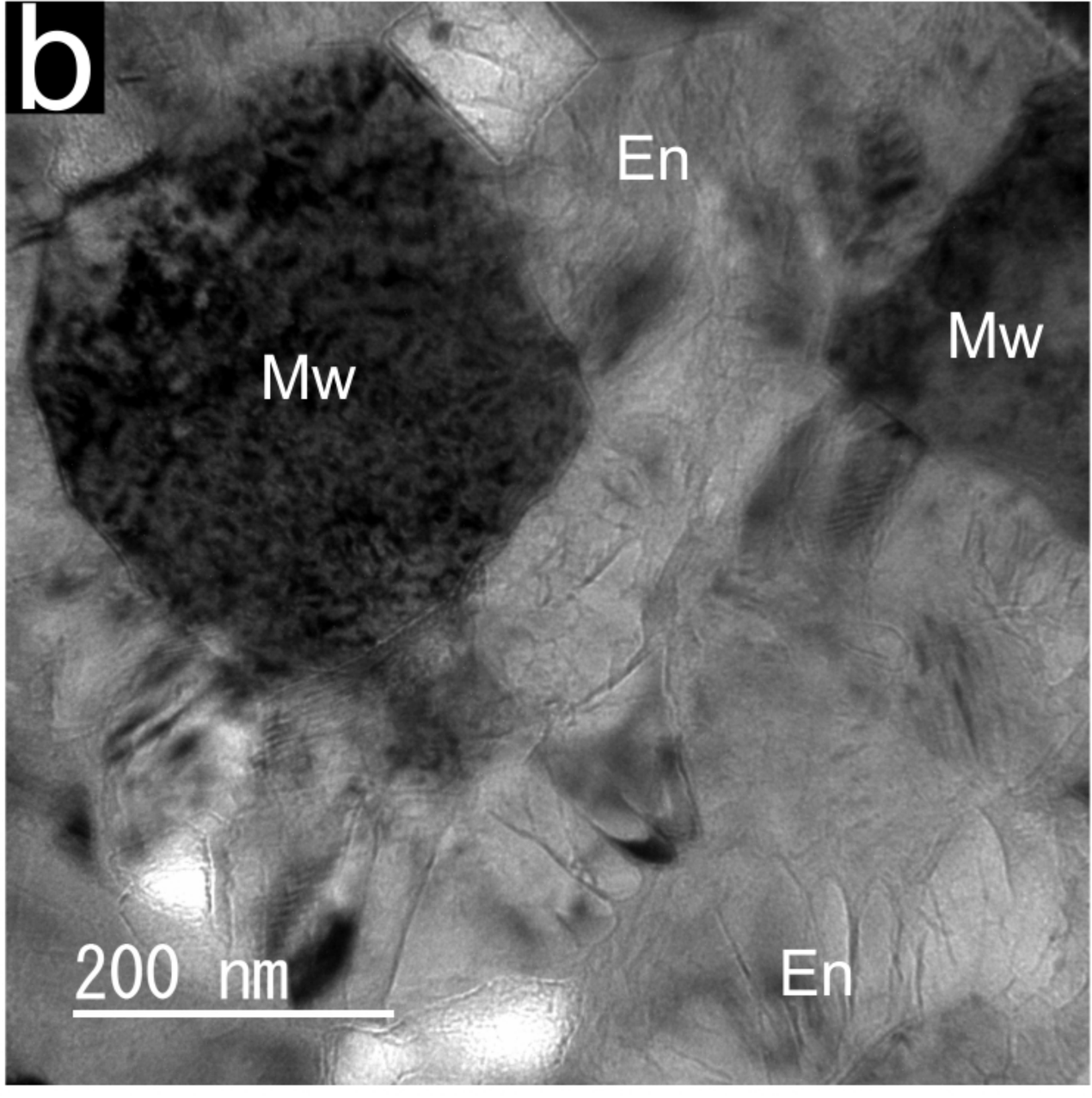
b
En
Mw
Mw
200 nm
En

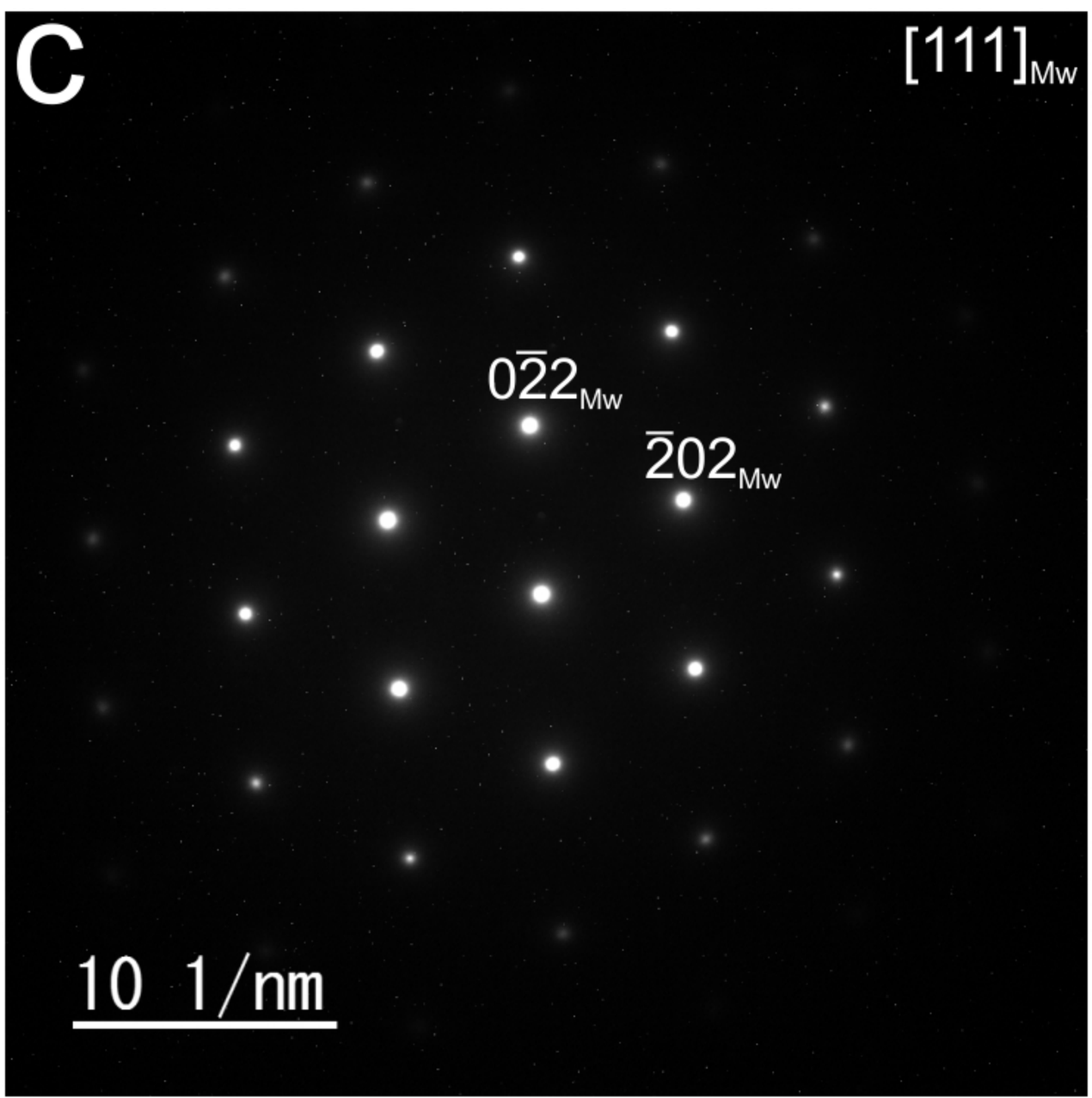
c
[111]Mw
0$\bar{2}$2Mw
$\bar{2}$02Mw
10 1/nm

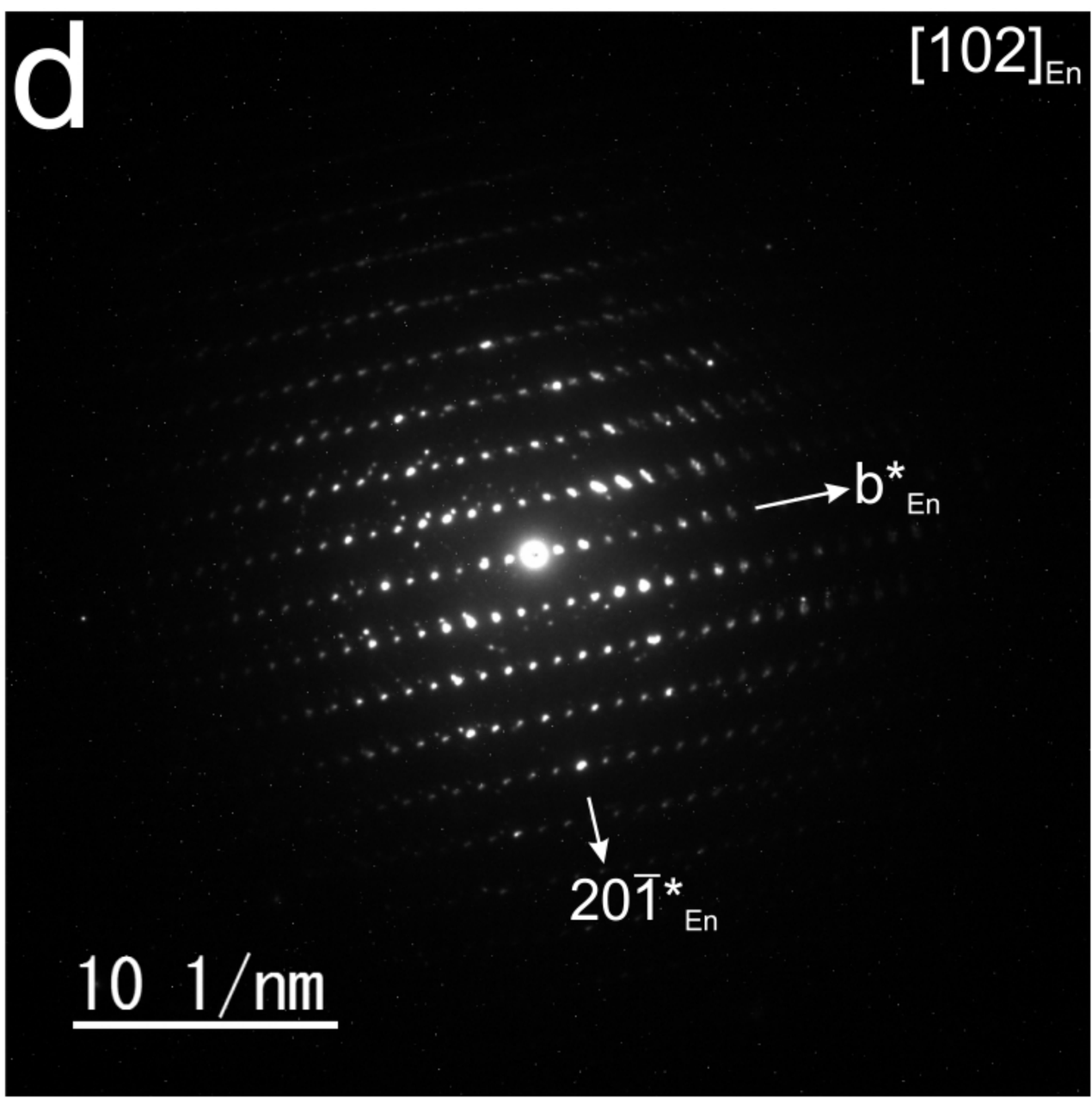
d
[102]En
b*En
20$\bar{1}$*En
10 1/nm